Fast thermal simulation of WAAM processing: toward manufacturing strategy evaluation

Nicolas Béraud, Yann Ledoux, El-Haddi Mechekour, Frédéric Vignat, Franck Pourroy

CIRP Journal of Manufacturing Science and Technology 55 (2024) 234–246

Contents lists available at ScienceDirect

CIRP Journal of Manufacturing Science and Technology

journal homepage: www.elsevier.com/locate/cirpj

Fast thermal simulation of WAAM processing: toward manufacturing strategy evaluation

Nicolas Béraud *, Yann Ledoux, El-Haddi Mechekour, Frédéric Vignat, Franck Pourroy

Institute of Engineering, Univ. Grenoble Alpes, CNRS, Grenoble INP, G-SCOP, 38000 Grenoble, France*

ARTICLE INFO

Keywords:
WAAM
Thermal simulation
Process simulation
Additive manufacturing

ABSTRACT

Managing the quality of parts produced by the Wire Arc Additive Manufacturing (WAAM) process presents a significant challenge, particularly due to the complexity of thermal control. Effective thermal management is crucial for minimizing defects, making fast and accurate thermal simulations essential for testing and optimizing various manufacturing strategies. This article proposes a rapid simulation that decouples the calculation of heat conduction from convection and radiation. The proposed simulation is described and validated against experimental data. The influences of spatial and temporal discretization are examined. In conclusion, this developed approach provides a fast and efficient simulation of a manufacturing strategy for improvement.

List of symbols

Symbols	Descriptions	Units
a	Surface of a voxel face	m^2
c	Specific heat capacity	J/(kg.K)
E(t)	Matrix of the energy field at time t	J
f	Function to convert energy to temperature	-
h	Heat transfer coefficient with air	W/(m^2. K)
I	Welding intensity	A
k_e	Heat kernel	-
M(t)	Matrix of the material field at time t	-
N	Number of elements deposited during the considered time step.	-
q(x,y,z)	Energy density of the Goldak heat source	J/m^3
Q	Welding energy input during a Δt time step	J
t	Current time	s
S(t)	Matrix of exchange surfaces	m^2
T	Temperature	K
T_{ini}	Initial temperature of the start plate	K
Δt	Time step	s
U	Welding voltage	V
V	Voxel volume	m^3
α	Thermal diffusivity	m^2/s
ε	Emissivity	-
λ	Thermal conductivity	W/(m.K)
η	Welding energetic efficiency	-
ρ	Density	kg/m^3
σ_B	Stefan-Boltzmann constant	kg.s^{-3}. K^{-4}

Notations.

Matrixis noted with a capital letter (e.g. M) and the element of this matrix with the indexes *i, j, k* will be noted $m_{i,j,k}$.

1. Introduction

The Wire Arc Additive Manufacturing (WAAM) process is a 3D metal-printing technique that enables the fabrication of parts by adding material. The material is fed to a welding torch in the form of wire and then melted using an electric arc. The movement of the torch can be controlled either by a CNC machine or a robot. The juxtaposition and stacking of weld beads create the 3D volume that forms the final part. One of the major advantages of this technique is its versatility allowing a high material deposition rate of material and the fabrication of complex shapes [1].

Controlling the quality of the parts produced by this process is critical, as a variety of defects can occur, including porosities, deformations, oxidation, cracking, residual stress and delamination [2]. These defects are primarily attributed to the thermal conditions during the fabrication of the part [3], necessitating precise thermal control to achieve near-net-shape geometry, as shown by [4]. Among the parameters affecting thermal conditions, idle time (also called dwell time) directly regulates the heat accumulation into the part by introducing a specific waiting time before adding the next layer. Several studies have shown the significant impact of this parameter on the quality of the produced geometry [5–7] have also highlighted the influence of the initial

* Corresponding author.
E-mail address: nicolas.beraud@univ-grenoble-alpes.fr (N. Béraud).

https://doi.org/10.1016/j.cirpj.2024.10.007
Received 12 April 2024; Received in revised form 20 September 2024; Accepted 10 October 2024
Available online 19 October 2024

temperature on the bead geometry. Additionally, [8,9] have investigated how the heat and material quantities influence the overall thermal state of the part, and consequently, its quality.

Thus, achieving a precise control of the thermal conditions is crucial for ensuring the quality of the produced parts. The literature highlights two main approaches for adjusting the value of these relevant parameters according to the expected thermal state within the part: in-process monitoring and thermal simulations.

In-process monitoring has been widely studied using various sensor technologies. Pyrometers offer valuable insights into real-time temperature monitoring within the part [10,11]. Other studies have focused on the use of cameras to monitor the temperature, often near the melt pool [12–14] or have explored the use of microbolometers [15–17] have proposed a closed-loop system to adjust the process parameters based on thermal measurements. Such a control can be integrated into commercial solutions [18]. While these methods enable real-time management of thermal conditions, they can be challenging to implement and do not allow for offline tuning of the process. Thermal simulations address this limitation by enabling comparison of different manufacturing strategies and optimization of process parameters [19]. Several models have been developed to simulate the WAAM process. These are mainly based on the finite element methods (FEM) [20–23] and some on the finite difference method [24]. Commercial software solutions, such as Simufact Additive [25], tackle this challenge, though simulating a 100 mm bead can take approximately 15 min for thermal analysis [26]. While these models are relevant and accurate, the required computation times remain significant. Since developing a manufacturing process often requires numerous iterations to identify the optimal manufacturing parameters, the current simulation times do not align with such uses. Reducing computation times would not only facilitate real-time process simulations but also open the door for integration with other learning-based methods.

Recent developments have introduced several approaches aimed at reducing computation time in thermal simulations. As an illustration, it can be cited the works of [27] using artificial neural networks to compute the thermal states based on process parameters, while [28] used a B-Spline model to enable quick interpolation of the thermal state. These approaches are promising but require extensive finite element simulations for training or model fitting, limiting their application to specific geometries. Mesh-free methods based on spectral graph theory [29] have been shown to cut computation time in half compared to FEM, but still fall short of the speed needed for practical use. Similarly, other techniques aimed at reducing FEM computation time as remeshing method [30].

The main scientific challenge lies in formulating thermal simulation methods for WAAM that are both fast and accurate, capable of accommodating various part geometries while facilitating quick optimization of process parameters. This paper tackles the issue by developing an original thermal simulation model for the WAAM process driven by rapid calculation times, conducive to offline process optimization of relevant manufacturing trajectories. These simulations could empower users or algorithms to refine manufacturing strategies, adjusting welding parameters, torch trajectories, or inter-layer waiting times. To achieve this, a rapid thermal simulation model is introduced including a sequential procedure to simulate the thermal conduction effect within the part and in parallel convection and radiation exchanges. The conduction is simulated through a Gaussian convolution calculation and leads to a drastic decrease of the computation times. The procedure is detailed in Section 3. A comparison with full finite element simulations and experimental data is provided in Section 4, validating the model's accuracy for WAAM operations. A quasi-real-time simulation is then obtained. A sensitivity analysis is performed in Section 5, examining the effects of mesh size and time step. Finally, we conclude with key insights and suggestions for future research directions.

2. Development of fast thermal simulation

Modeling the WAAM process is a challenging task requiring the management of various complex factors. These include the continuous addition of material, the movement of the heat source for fusing the material, the variation of material properties over a large range of temperatures, and the modeling of the built plate, gas flow, and substrate characteristics. Different approaches can be identified in the literature to manage a balance between computational efficiency and accuracy. Recent works have implemented spatial and temporal adaptative discretizationsto meet this critical objective [30,31]. Additionally, advancements in numerical schemes, such as those proposed by [32] for additive manufacturing processes (specifically powder bed fusion), have shown potential in improving the efficiency of additive manufacturing simulations. A state of-the art is available in the work of [33].

The main originality of this study lies in two key aspects. Firstly, it involves parallel computation of heat conduction within the part and the built plate, along with heat losses due to radiative and convective phenomena. Second, the temperature field evaluation is based on convolution product assuming a heat kernel function and Gaussian distribution through the material over time. This section describes the developed simulation process, including discretization method, state initialization, and temporal evolution modeling. Fig. 1 shows a typical example of manufactured geometry and the associated mesh used for its simulation. The full manufacturing space is drawn in green color, and the starting plate (the base structure where metal will be added) and the manufactured part (a central wall) depicted in blue. To make more tractable the numerical computation and straightforward implementation, the simulation method is formulated in matrix form. This approach leverages widely available libraries for efficient matrix calculations.

2.1. Discretization

To compute the temperature field at any given point and time, different steps and assumptions are required. The first step consists of the discretization of the full manufacturing space into voxels as depicted in Fig. 1. In the present case, the voxels are cubic in shape, simplifying the use of regular matrices to represent spatial fields. Time is discretized using a time step of Δt. Thus, the manufacturing space is modeled by two matrices for each time step:

- A matrix representing the material filling information for each voxel at the date t:

$$\mathrm{M}(t)$$

$$\text{with } \mathrm{m}(t)_{xyz} = 1 \leftrightarrow \textit{voxel filled with material}$$

$$\textit{and } \mathrm{m}(t)_{xyz} = 0 \leftrightarrow \textit{empty voxel} \tag{1}$$

  Where x, y, z represents the coordinates of the center of the considered voxel.
- A matrix representing the energy of each voxel:

$$\mathrm{E}(t)$$

$$\begin{array}{l} \textit{such as } \mathrm{m}(t)_{xyz} = 0 \rightarrow \mathrm{e}(t)_{xyz} = 0 \\ \textit{and if } \mathrm{m}(t)_{xyz} = 1 \rightarrow \mathrm{e}(t)_{xyz} \neq 0 \end{array} \tag{2}$$

2.2. State initialization

The material and energy matrices are initialized at time $t = 0$, representing the substrate upon which the part will be manufactured. For all voxels representing the substrate $\mathrm{m}(0)_{xyz}$ is set to 1 and the energy is defined according to Eq. 3.

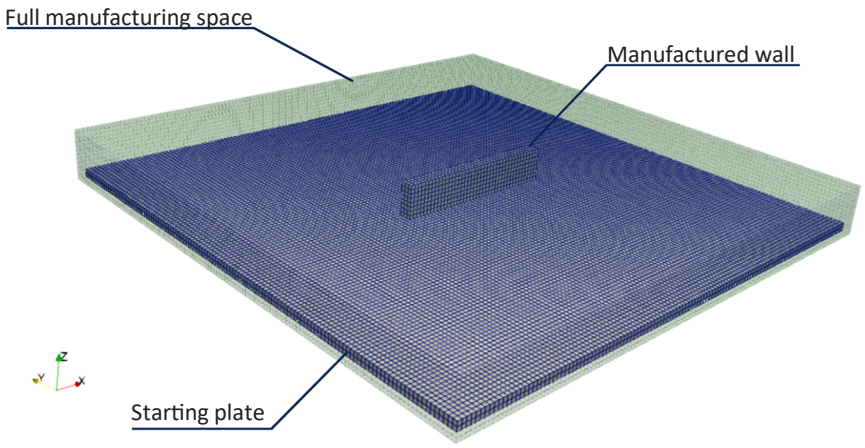

Fig. 1. Description of the manufacturing space.

$$\text{For all } (x,y,z) \text{ such as } m(0)_{xyz} = 1 \text{ then } e(0)_{xyz} = \rho(T).c(T).V.T_{ini} \quad (3)$$

Where $\rho(T)$ and $c(T)$ represent the density and the specific heat capacity as a function of the temperature, V is the voxel volume, T_{ini} is the initial temperature of the start plate and $e(0)_{xyz}$ corresponds to the energy of a voxel at the initial temperature.

2.3. Temporal evolution modeling

Several phenomena must be modeled to compute the temperature field of the part during the WAAM process, including:

- Material and energy input from the welding torch
- Energy loss from the part through convection and radiation
- Heat diffusion by conduction

One of the major proposals of this article for significantly reducing calculation times is to separate the solving of the diffusion equation from the calculation of radiation and convection with the external environment. Fig. 2 shows the process to obtain the energy and material matrix at step time $t + \Delta t$. The following paragraphs describe the procedure in detail.

2.3.1. Welding simulation

Both material inputs (from the molten wire) and energy input (from the electric arc) need to be modeled to simulate the welding process.

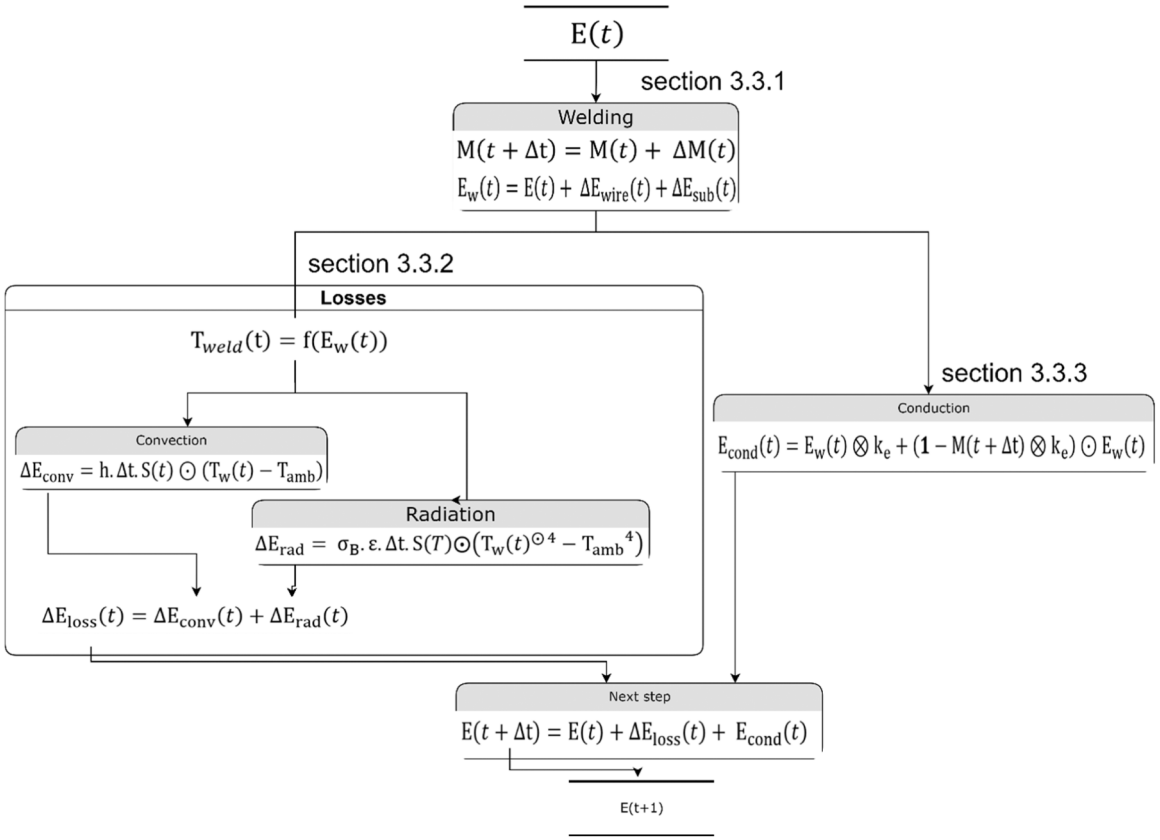

Fig. 2. Simulation process for calculating E(t + Δt).

First, the matrix $\Delta M(t)$ is created with the same size as the matrix $E(t)$ and with all its elements set to 0, except those that have received material between t and $t+\Delta t$ which are set to 1. Then the matrix $M(t+\Delta t)$ can be expressed as in Eq. 4.

$$M(t+\Delta t) = M(t) + \Delta M(t) \tag{4}$$

Researches have focused on modeling the heat input of MIG processes [34,35]. The energy distribution between the wire and the substrate is well documented [22,36,37]. The useful power of the welding station (Q) can be expressed as:

$$Q = \eta.U.I.\Delta t \tag{5}$$

Where U represents the welding voltage, I the welding intensity and η the welding energetic efficiency. The total welding energy is divided into two components: one for heating the wire (Q_{wire}), and another for heating the substrate (Q_{sub}). Based on previous studies ([22], [37]), the sum of the two contributions equals the total useful energy of the welding process (Q), which is assumed to be equally distributed between them:

$$Q = Q_{wire} + Q_{sub} \tag{6}$$

$$Q_{wire} = Q_{sub} = \frac{1}{2}Q \tag{7}$$

The energy of the deposited elements is assigned through the matrix $\Delta E_{wire}(t)$, matrix with the same size as $E(t)$ and its elements are defined by Eq. 8.

$$\Delta E_{wire}(t) = \frac{Q}{2N}\Delta M(t) \tag{8}$$

Where N is the number of deposited elements during the time step.

[34] has shown that the energy brought to the substrate can be modeled as a double ellipsoid. This can be discretized into the $\Delta E_{sub}(t, t+\Delta t)$ matrix, which has the same dimensions as $E(t)$, defined by the Eqs. 9 and 10.

$$\Delta e_{subxyz}(t) = \int_{Voxel} q(x,y,z)dV \tag{9}$$

$$\frac{Q}{2} = \sum_{\text{Manufacturing space}} \Delta e_{subxyz}(t) \tag{10}$$

Where $q(x,y,z)$ represents the energy density distribution as defined in the literature (a double ellipsoid distribution centered on the welding point). Thus, the energy matrix after the welding modeling ($E_w(t)$) can be expressed by Eq. 11.

$$E_w(t) = E(t) + \Delta E_{wire}(t) + \Delta E_{sub}(t) \tag{11}$$

2.3.2. Energy loss

Conduction through contact with external solids such as clamping system or the manufacturing table, is not considered in this study. With this assumption, the model represents a part isolated from other components by refractory elements. So, the energy loss in the modeled part occurs solely through two mechanisms: convection and radiation. The matrix $\Delta E_{loss}(t)$ represents the energy loss during the time step as the sum of $\Delta E_{conv}(t)$, corresponding to the energy lost by convection and $\Delta E_{rad}(t)$ corresponding to the energy lost by radiation (Eq. 12).

$$\Delta E_{loss}(t) = \Delta E_{conv}(t) + \Delta E_{rad}(t) \tag{12}$$

First, it is necessary to calculate the temperature field $T_{weld}(t)$ from the energy matrix. The link between energy and temperature is a bijective function that can be established using material properties ($\rho(T)$, $c(T)$, V) as described in equation 13. This bijection is illustrated Fig. 1..

Thus, the part temperature field $T_{weld}(t)$ is calculated from the energy matrix using Eq. 13.

$$e_w(t) = \int_0^{T_{weld}(t)} \rho(T).c(T).V.dT$$

and

$$T_{weld}(t) = f(E_w(t)) \tag{13}$$

The specific latent heat required for the phase change is also included in the evolution of $c(T)$, ensuring appropriate modeling of the phase change.

The exchange due to convection (ΔE_{conv}) is calculated as described in Eq. 14.

$$\Delta E_{conv} = h.\Delta t.S(t) \odot (T_w(t) - T_{amb}) \tag{14}$$

Where $\odot$ is the Hadamard product, h is the transfer coefficient with air (assumed to be constant regardless of the temperature), T_{amb} is the ambient temperature and $S(t)$ is the matrix with the same dimensions as $M(t)$, where each element contains the free surface area of the corresponding voxel. Each element of $S(t)$ is calculated as the product of the area of a voxel face and the number of free faces (those in contact with air). The calculation for each element of the S(t) matrix is detailed in Eq. 15.

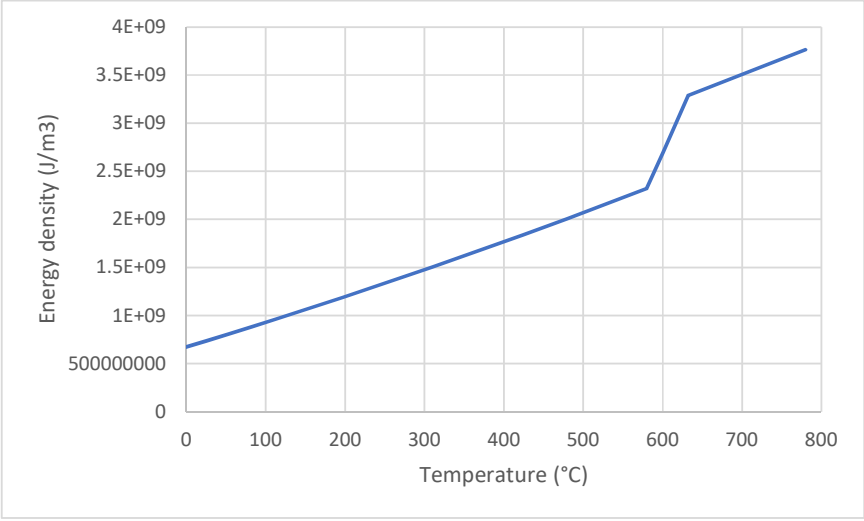

Fig. 3. Bijection between temperature and energy density.

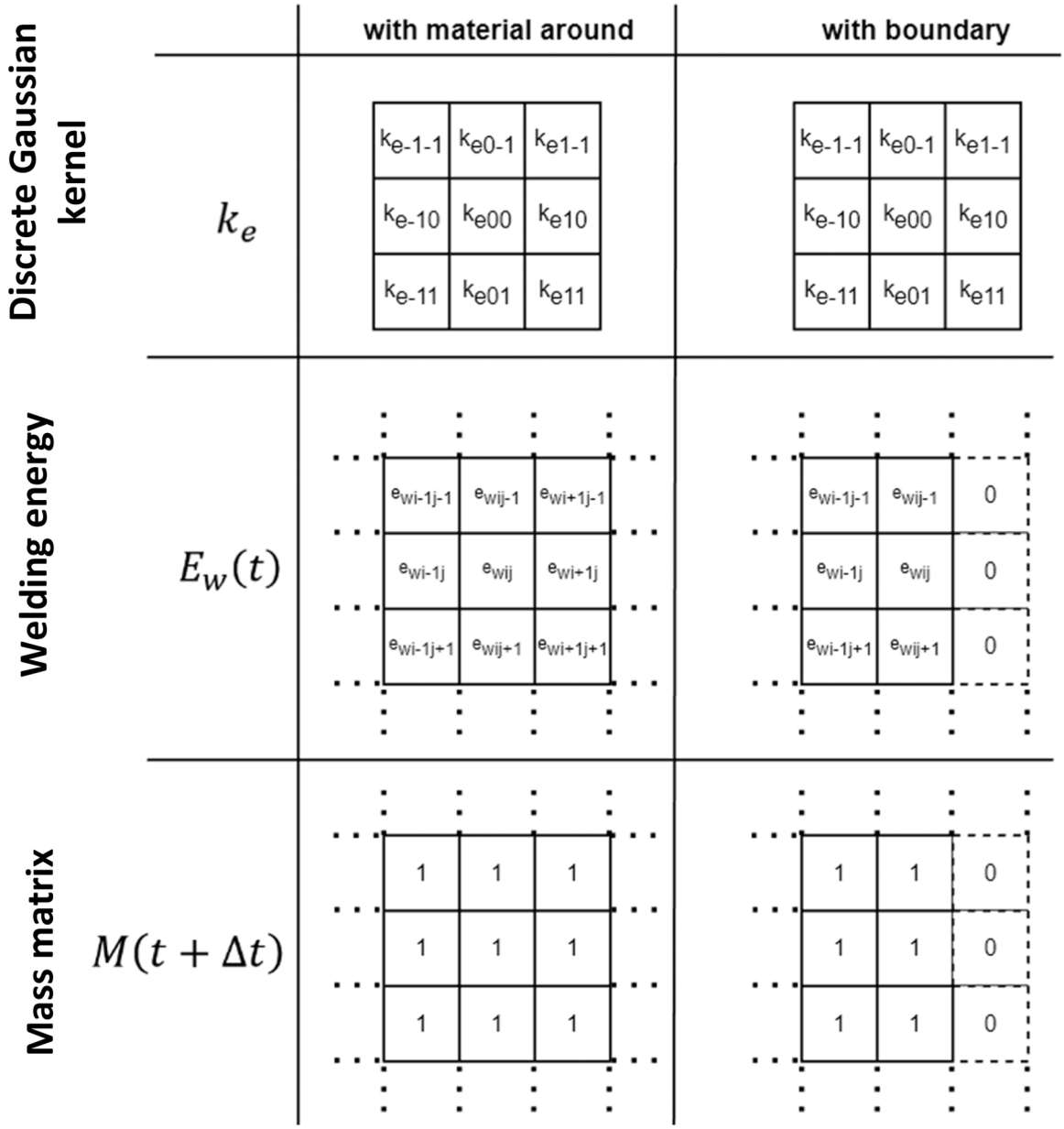

Fig. 4. Illustration of Eq. 22 on a 2D example for finite and infinite domains.

$$s(t)_{xyz} = a\Big(m(t)_{x+1yz} + m(t)_{x-1yz} + m(t)_{xy+1z} + m(t)_{xy-1z} + m(t)_{xyz+1} + m(t)_{xyz-1}\Big) \tag{15}$$

Where a is the surface area of one face of a voxel.

To simplify the calculation of radiation, it is assumed that all energy is radiated outward to the workspace's exterior at the temperature T_{amb}. This approximation is effective for simple shapes with few sharp edges, but may introduce more significant errors for complex geometries. These assumptions lead to the formulation of Eq. 16.

$$\Delta E_{rad} = \sigma_B.\varepsilon.\Delta t.S(T) \odot \left(T_w(t)^{\odot 4} - T_{amb}{}^4\right) \tag{16}$$

Where $\odot$ is the Hadamard power, σ_B is the Stefan-Boltzmann constant, ε the emissivity (being constant regardless of the temperature).

2.3.3. Conduction calculation

An analytical solution for heat conduction is studied to enable a fast calculation. The heat equation is established under three hypotheses as outlined by [38]:

- Adiabatic condition: no exchange with the external environment.
- Constant material properties: thermal conductivity (λ), density, and specific heat capacity are assumed to remain independent of both position and temperature.
- Infinite domain.

Since the simulation of heat input and heat losses are simulated separately (as shown in Fig. 2), the system can be considered adiabatic during the conduction calculation phase. To simplify the use of the analytical solution, thermal properties such as conductivity, density, and thermal capacity are assumed to be constant. These properties are set to values corresponding to the liquidus temperature, as this temperature represents the point where the thermal gradient is most pronounced near the weld bead, where conduction is most significant. This assumption will be further addressed in Section 5. Under the adiabatic condition, with constant material properties and an infinite domain,

heat conduction is governed by the heat equation which corresponds to a standard wave equation (Eq. 17).

$$\frac{\partial u}{\partial t'} = \alpha \nabla u \tag{17}$$

$$u(t' = 0) = u_0 \tag{18}$$

Where u is the energy field, ∇ is the Laplacian operator, and the thermal diffusivity $\alpha = \lambda_1/(\rho_1 c_1)$. A known solution of this equation is given in Eq. 19 [38].

$$u(x, t') = \frac{1}{\sqrt{4\pi K t'}} \int_{-\infty}^{+\infty} e^{-\frac{(x-x')^2}{4\alpha t'}} u_0 dx' \tag{19}$$

This equation asserts that the solution to the heat transfer at time t' is the convolution of the initial data u_0 with the Gaussian kernel. This can be expressed in a discretized field according to Eq. 20.

$$u(t') = u_0 \otimes k_{e'} \tag{20}$$

Where $\otimes$ is the convolution operator and $k_{e'}$ is the heat kernel for the evolution between date 0 and t'. The heat kernel ($k_{e'}$) is a Gaussian kernel with a standard deviation $\sigma' = \sqrt{\alpha t'}$.

Eq. 21 extends this equation to a discrete field and by considering $u_0 = E(t)$ and $t' = t + \Delta t$.

$$E_{cond}(t) = E_w(t) \otimes k_e \tag{21}$$

With k_e the heat kernel between t and $t+\Delta t$ corresponding to a Gaussian kernel with a standard deviation $\sigma = \sqrt{\alpha \Delta t}$. Eq. 21 is valid for an infinite domain.

For simulating the manufacturing of finite parts, the equation needs to be adjusted to take into account the adiabatic boundary condition on a bounded domain. Eq. 21 is adapted with an additional term as shown in Eq. 22.

$$E_{cond}(t) = E_w(t) \otimes k_e + (\mathbf{1} - M(t + \Delta t) \otimes k_e) \odot E_w(t) \tag{22}$$

With **1** being a matrix with the same dimensions as M and entirely filled with 1. For a voxel fully surrounded by material, the solution is equivalent to that of an infinite domain. Indeed, for a voxel of at the center *x, y, z*, fully surrounded by material $m(t + \Delta t)_{xyz} \otimes k_e = 1$. Furthermore, this equation validates the energy conservation (Eq. 23).

$$\sum e_{condij} = \sum e_{wij} \tag{23}$$

To verify Eq. 22, let's illustrate it with a 2D example using a 3 × 3 kernel for both infinite and finite solutions.

The following equations show all occurrences of the term e_{wij}

– For infinite domain:

The terms of $E_{cond}(t)$ including occurrences of e_{wij} can be expressed as:

$$e_{condi-1j-1} = \ldots + e_{wij} k_{e11}$$

$$\ldots$$

$$e_{condij} = \ldots + e_{wij} k_{e00} + \ldots$$

$$\ldots$$

$$e_{condi+1j+1} = e_{wij} k_{e-1-1} + \ldots \tag{24}$$

By summing all the e_{condij}, we obtain:

$$\sum e_{cond\ ij} = e_{w\ ij} \sum_{\substack{m\in\{-1,0,1\} \\ n\in\{-1,0,1\}}} k_{e\ mn} + \ldots \tag{25}$$

By definition, the sum of all the terms of the heat kernel is equal to 1. So, we obtain the equation:

$$\sum e_{condij} = e_{wij} + \ldots \tag{26}$$

So, by proceeding in the same way for all e_{wij}, we obtain Eq. 23 allowing to verify the energy conservation.

– For bounded domain

By applying Eq. 22, terms of $E_{cond}(t)$ including occurrences of e_{wij} can be expressed as:

$$e_{condi-1j-1} = \ldots + e_{wij} k_{e11} + \ldots$$

$$e_{condi-1j} = \ldots + e_{wij} k_{e\ \ 10} + \ldots$$

$$e_{condi-1j+1} = \ldots + e_{wij} k_{e1-1} + \ldots$$

$$e_{condij-1} = \ldots + e_{wij} k_{e01} + \ldots$$

$$e_{condij} = \ldots + e_{wij} k_{e00} + \ldots + [1 - (k_{e-1-1} + k_{e0-1} + k_{e-10} + k_{e00} + k_{e-1-1} + k_{e0-1})] e_{wij}$$

$$e_{condij-1} = \ldots + e_{wij} k_{e0-1} + \ldots$$

$$e_{condi-1j+1} = 0$$

$$e_{condij+1} = 0$$

$$e_{condi+1j+1} = 0 \tag{27}$$

By summing all the e_{condij}, we obtain the equation:

$$\sum e_{cond\ ij} = e_{wij} \sum_{\substack{m\in\{0,1\} \\ n\in\{-1,0,1\}}} k_{e\ mn} + \left[1 - \sum_{\substack{m\in\{-1,0\} \\ n\in\{-1,0,1\}}} k_{e\ mn}\right] e_{w\ ij} + \ldots \tag{28}$$

As the Gaussian kernel is symmetric, so $k_{emn} = k_{e\ -mn}$, and then:

$$\sum_{\substack{m\in\{0,1\} \\ n\in\{-1,0,1\}}} k_{emn} = \sum_{\substack{m\in\{-1,0\} \\ n\in\{-1,0,1\}}} k_{e\ mn} \tag{29}$$

Eq. 28 can be simplified as follows:

$$\sum e_{cond\ ij} = e_{w\ ij} + \ldots \tag{30}$$

By applying the same approach to all e_{wij}, we derive Eq. 23. Extending this method to three dimensions for each e_{wijk}, we show energy conservation as defined in Eq. 23.

2.3.4. Calculation of next step energy

The evolution of energy at time step $t+\Delta t$ can be calculated from previous values as shown in Eq. 31.

$$E(t + \Delta t) = E(t) + \Delta E_{loss}(t) + E_{cond}(t) \tag{31}$$

By following the outlined procedure for each calculation step, the manufacturing process of a part can be effectively simulated. The matrix formulation simplifies implementation and enables fast calculation using Python and dedicated libraries such as *numpy* and *scipy*. The heat kernel convolution is easily calculated through the standard Gaussian filter functionality from the *ndimage* module. Since the material's thermal properties are assumed constant for the conduction, a fixed kernel size can be used, allowing the application of standard algorithms. Fig. 5 illustrates an example of the resulting temperature field at a specific time step.

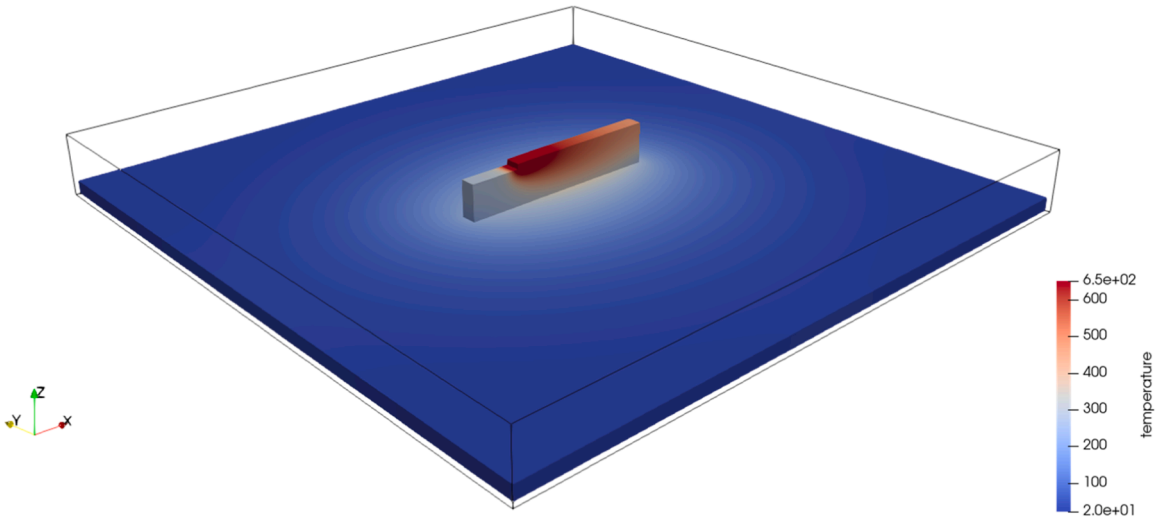

Fig. 5. Example of temperature field at a given time step.

3. Comparison with reference values

This section has two main objectives: first, to assess the accuracy of the proposed simulation method by comparing it with experimental data, and second, to evaluate its computation time relative to a standard FEM approach. For this purpose, it is used the work of [36], which presents a benchmark case involving the construction of a thin wall. This study provides both experimental data and simulation results for the manufacturing processes. The experimental data will be used to qualify the accuracy of the proposed method, while the simulation results will serve to quantify the reduction in computation time compared to the FEM simulation.

3.1. Validation case

3.1.1. Experimental setup

The proposed experiment is the manufacturing of an 8-layer wall using a zigzag welding strategy. The wall is built with a Yaskawa MA1440 six-axis robot equipped with a two-axis positioner and a Fronuis T.P.S. CMT 4000 Advanced welding station (Fig. 6). The wall is made from aluminium alloy Al5356 and is built on a 250 mm × 250 mm × 5 mm Al5083 substrate, initially maintained at 20 °C. To prevent conduction with external solids, the substrate is placed on firebrick, ensuring that energy loss occurs only through convection and radiation.

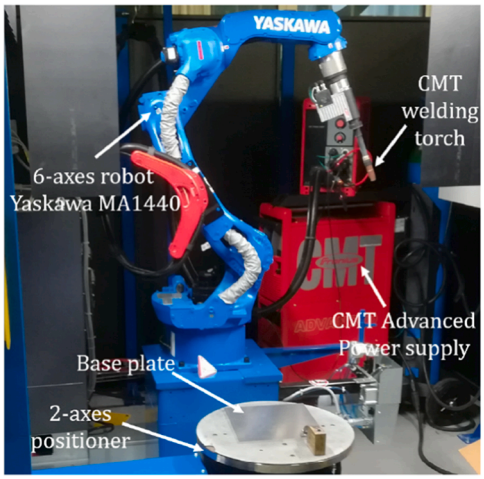

Fig. 6. Experimental WAAM system.

Key welding parameters, such as input power, travel speed, idle time, acquisition duration, synergic Wire Feed Speed (WFS), and the balance between Electrod Positive and Electrod Negatif (EP/EN) cycles are detailed in Table 1. Fig. 7 illustrates the experimental setup, with six thermocouples (P1 to P6) are placed to record the surface temperatures of the part, with a data acquisition frequency of 4 Hz. These temperature measurements will be used to validate the thermal simulation results.

3.2. Fast thermal model setup

The voxel size is set to 1 mm × 1 mm x 1 mm and the time step is 0.1 s. These values are consistent with those used in the finite elements model described in [36], allowing a reliable comparison of calculation time. The influence of these values will be discussed in the Section 5. To maintain consistency with the reference [36], all other parameters, including thermal-dependant thermal properties, are adopted from [39]. These properties are used to establish the bijection between energy density and temperature. As detailed in the dedicated section on conduction simulation, the size of the heat kernel is determined by material properties that are assumed constant. In this case, properties at the liquidus temperature are selected (Table 2). Goldak heat source parameters, used to define $\Delta E_{sub}(t)$ values, are also chosen to align with the reference data in [39]. The welding efficiency energy (η) is set to 0.83 [39], and the emissivity is set to 0.77, in agreement with [40].

3.3. Results

As previously depicted, the values from [36] will be used as the reference for this study. This reference provides temperature measurements from six thermocouples during the manufacturing of the wall, as well as the calculation time to simulate the same manufacturing through a standard FEM model. The proposed simulation will be compared on two sides: firstly, on accuracy, and secondly on calculation.

3.3.1. Accuracy

One objective of the developed simulation is to be used to optimize process parameters. In this section, we evaluate the accuracy of the simulated temperature fields by comparing them to experimental data. Fig. 8 shows the temperature evolution at points P1 to P6, where dashed lines represent experimental values and solid lines correspond to simulated values. For each point, the mean absolute deviation and the Pearson coefficient are calculated. The Pearson coefficient is particularly relevant for validating both the amplitude and synchronization of two curves. Table 4 summarizes these results, showing that the maximum

Table 1
Manufacturing parameters.

Parameters	Input power (U.I)	Travel speed	Idle time	Acquisition duration	Synergic WFS	EP/EN	Synergy law
Units	W	mm/s	s	s	m/min		CMT advanced
Values	960	10	2	170	5	+1	1368

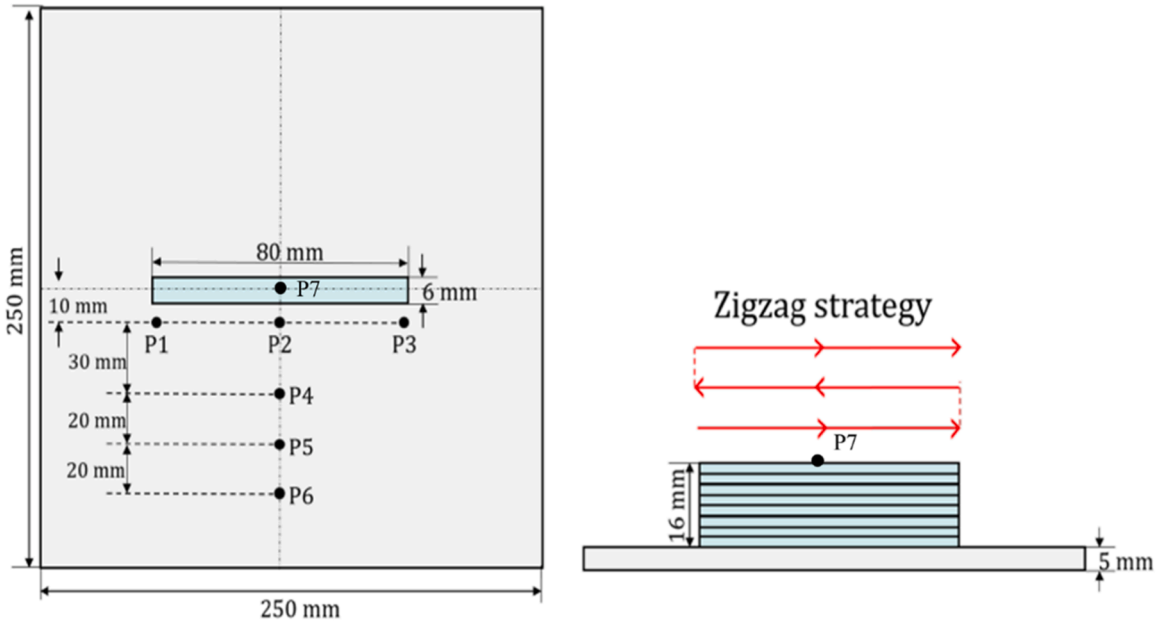

Fig. 7. Experimental design [36].

Table 2
Material properties [39].

Properties	c_l	λ_l	ρ_l	h	ε	η
Units:	J/(kg.K)	W/(m.K)	kg/m^3	W/(m^2. K)	-	-
Values:	1261	177	2549	20	0.77	0.83

mean deviation occurs at point P2, with a deviation of 32.1 °C, while the lowest Pearson coefficient is 0.897 at point P4. Across all six points, the average Pearson coefficient is 0.957, and the average of the mean absolute deviation is 20.2 °C.

Points P1 and P3 exhibit half the number of temperature peaks compares to P2, as they are located near the half-turn generated by the zigzag welding strategy. This results in a noticeable asymmetry at P1 and P3, reflecting the approach and departure of the welding torch. These characteristics are observed in both the simulated and measured data. Additionally, the cooling rates and asymptotic temperature values are well aligned between the two datasets, indicating good consistency.

3.3.2. Calculation time

Both simulations were executed on the same computer equipped with an Intel Core i7–8700 CPU @ 3.20 GHz corresponding to 0.38 TFLOPS. For an experimental duration of 170 s, the FEM simulation proposed by [36] required 12 000 s of computation time. In contrast, the proposed simulation completed in 150 s, making it 80 times faster than the reference FEM simulation and 1.13 times faster than the real process.

In comparison, commercial software like Simufact have a calculation time about 15 min to simulation 100 mm of trajectory in thermal simulation [26]. Given that the studied case involves a 640 mm trajectory, this would result in an estimated calculation time of over 5 760 s, making this approximately 38.4 times slower than the proposed simulation, excluding the cooling phase.

4. Discussion

4.1. Comparison with FEM and experiment

In terms of accuracy, the proposed simulation exhibits performance compatible with the objective of optimizing manufacturing parameters. According to [41], a 100 °C variation in substrate temperature can result in a change of approximately 0.5 mm in the deposited bead radius. Therefore, the mean deviation of about 20 °C observed in the proposed simulation is within an acceptable range. Moreover, the largest deviations are observed during temperature peaks while the overall curves do not seem to drift, validating the model's energy balance. Currently, all parameter values are based on literature findings for both material and process conditions. Calibrating these parameters based on the experimental data could further improve accuracy, particularly in the evaluation of the heat transfer coefficients and welding efficiency.

From a computational perspective, the proposed simulation offers a significant time advantage over traditional finite element methods, making it highly suitable for use in optimizing manufacturing parameters, even in iterative processes. Additionally, its ability to run faster than real time presents the opportunity for real-time adjustments during the manufacturing process.

4.2. Influence of spatial and time discretization

The influence of time and spatial discretization on simulation accuracy and efficiency is examined. A reference configuration is selected with a time increment of 0.1 s and a voxel size of 1 mm. Three criteria are analyzed for this comparison: the mean absolute deviation between calculated and measured temperatures at points P1 to P6, the mean Pearson coefficient between calculated and measured temperatures at these points, and the computing time on a given computer (detailed in section 4.2.2). Variations in time increment are assessed with steps of

Table 3
Comparison of experimental and simulation results.

Point:	P1	P2	P3	P4	P5	P6	Mean on all points
Mean absolute deviation (°C)	19.2	32.1	13.6	14.2	19.5	23.2	20.2
Mean Pearson coefficient	0.983	0.984	0.983	0.897	0.942	0.956	0.957

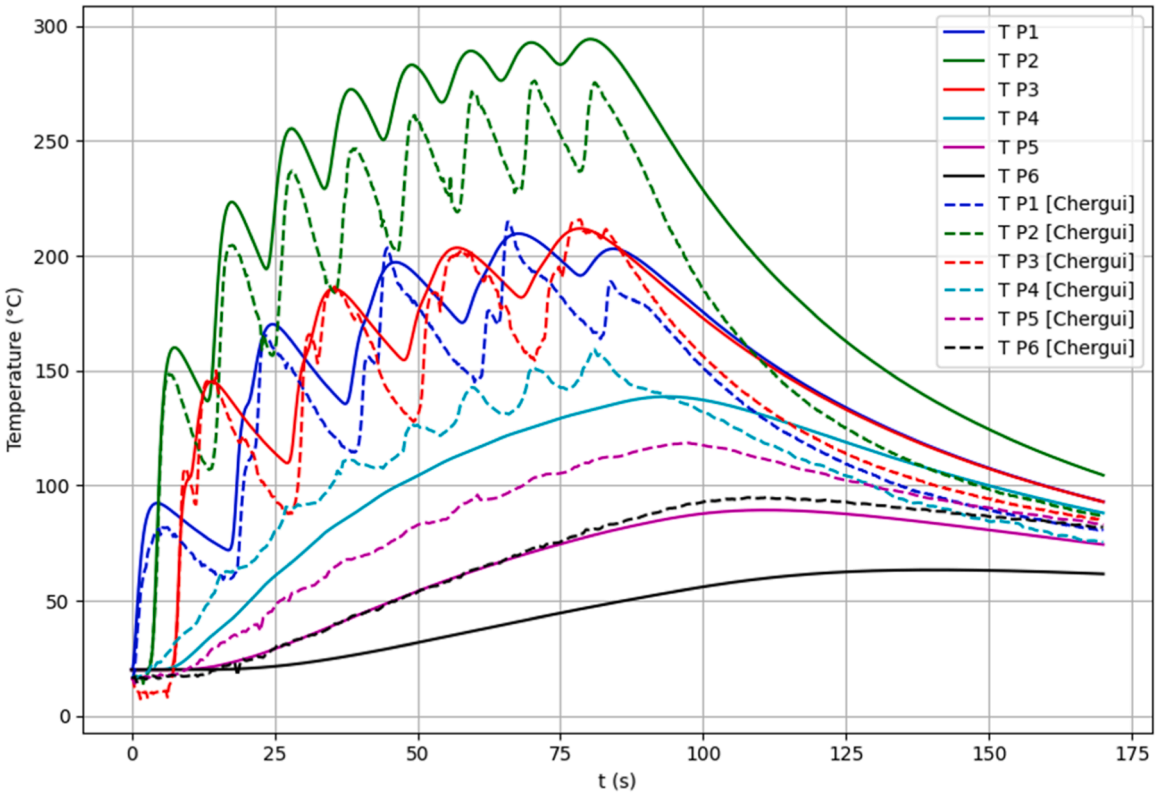

Fig. 8. Comparison between experimental values from [36] and values from developed simulation.

0.05, 0.1, and 0.2 s, while different spatial discretization are tested with voxel sizes of 0.25, 0.5, and 1 mm. Table 4 presents the effects of these parameters on the three criteria with the first row representing the performance of the initial simulation setup.

The time step has a significant impact on the mean absolute deviation, with smaller time steps enhancing model accuracy, validated by a Pearson coefficient greater than 0.923, which indicate good frequency synchronization. Increasing the time step slightly degrades this indicator. As expected, the computing time is closely related to the time step (Fig. 9). The voxel size, however, shows a negligible effect on the model quality (mean absolute deviation and Pearson coefficient) within the tested range. Computing time is mainly proportional to the number of voxels, as expected (Fig. 9).

Points P1 to P6, though located at some distance from the welding torch, provide useful comparison with experimental values. For process optimization, the temperature field near the last layer is crucial. Therefore, the impact of discretization on the temperature of the last layer temperature will be evaluated. This involves monitoring the temperature at point P7 over time after its activation (i.e. after the welding torch has passed). Fig. 10 illustrates how discretization affects this temperature, showing that the influence near the electric arc is significantly the same as on other control points.

Table 4
Influence of time and spatial discretization.

Time step (s)	Voxel size (mm)	Mean absolute deviation (°C)	Mean Pearson coefficient	Number of elements	Calculation time (s)
0.1	**1**	**20.2**	**0.958**	**1 587 600**	**150**
0.05	0.5	17.0	0.968	12 096 192	2559
0.2	0.5	24.4	0.923	12 096 192	1057
0.1	0.25	19.7	0.951	94 376 376	19961
0.1	0.5	19.5	0.954	12 096 192	1519

4.3. *Influence of heat kernel size*

According to the developed numerical scheme, the kernel size remains constant during the conduction calculation regardless the temperature evolution. It corresponds to the liquidus state. It is proposed to study the modification of these properties according to the temperature evolution.

Table 5 shows the evolution of material properties for both ambient temperature (25 °C) and liquidus temperature (580 °C) according to [39]. It illustrates the evolution of the heat kernel standard deviation and the influence on the mean absolute deviation and the mean Pearson coefficient. Fig. 11 shows the influence of the heat kernel standard

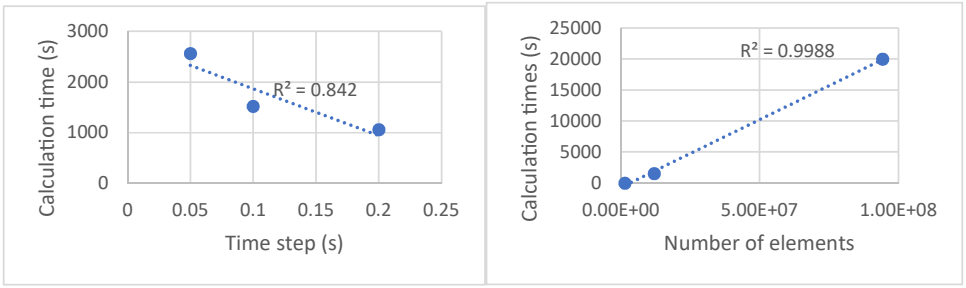

Fig. 9. Evolution of computing time according to time step and number of elements.

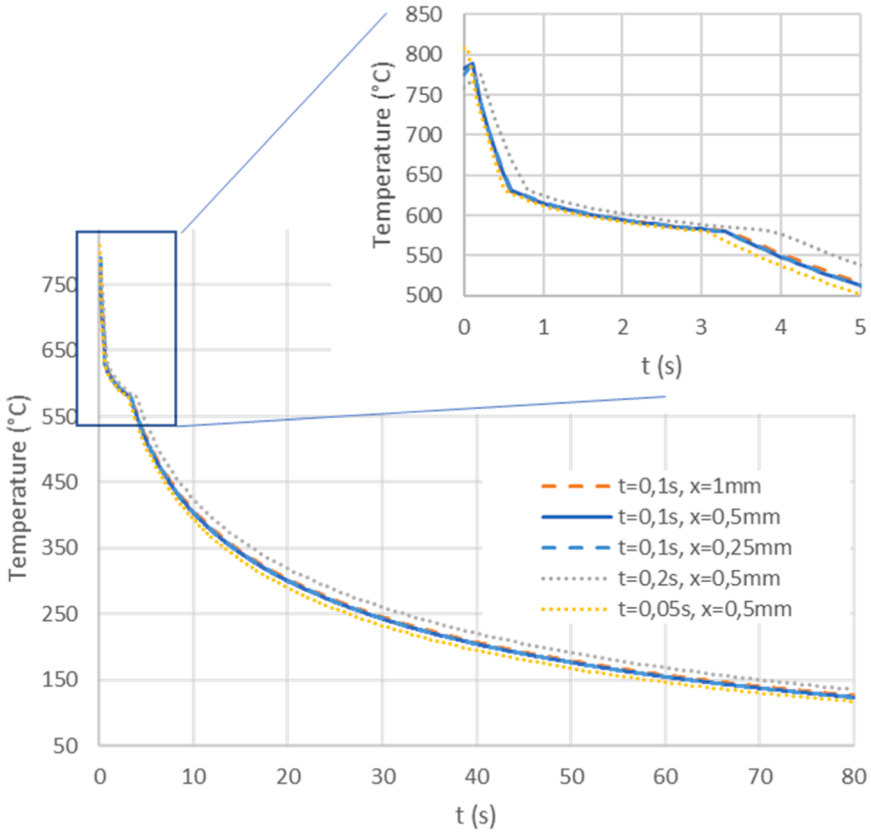

Fig. 10. Influence of discretization on temperature at point P7.

Table 5
Material properties according to temperature.

Properties	T	c	λ	ρ	σ	Mean absolute deviation	Mean Pearson coefficient
Units:	°C	J/(kg.K)	W/(m.K)	kg/m^3	-	°C	
	25	1096	144.6	2604	1.56.10^{-3}	22.6	0.940
	580	1261	177	2549	1.66.10^{-3}	19.5	0.954

deviation for material properties at 25 and 580 °C over time at point p7. On all criteria, this influence remains very low validating the hypothesis of maintaining constant material property during conduction calculation.

4.4. Calculation time

Fig. 12 shows the distribution of the cumulative percentage of times spent in each of the functions during model solving. Conduction simulation accounts for 60.2 % of the cumulative computation time. Even if the duration of the simulation is considerably shorter compared to FEM one, improvements are possible:

- Parallelizing conduction and heat loss calculation could save approximately 20 % of calculation time. Currently, these operations are not parallelized, even though there is no dependency between them. This will be a future improvement.
- Implementing more suitable data structures than matrices could reduce the number of elements describing space without material. For a voxel size equal to 1 mm, the matrix contains 1 587 600 elements, with 77 % being zero elements (corresponding to the surrounding area of the built plate, green zone in Fig. 1). Using a more

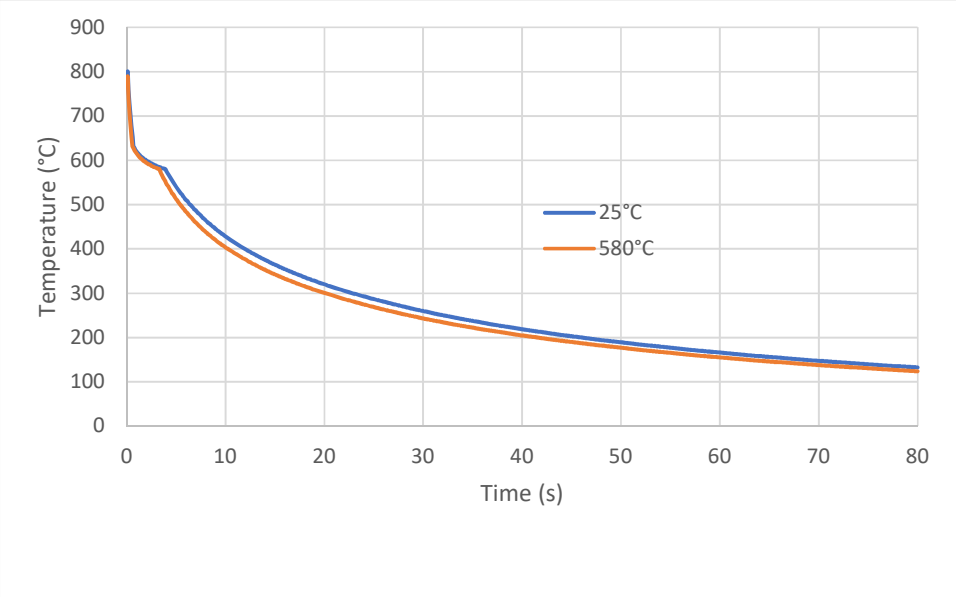

Fig. 11. Influence of heat kernel standard deviation for material properties at 25 and 580 °C on temperature of point P7.

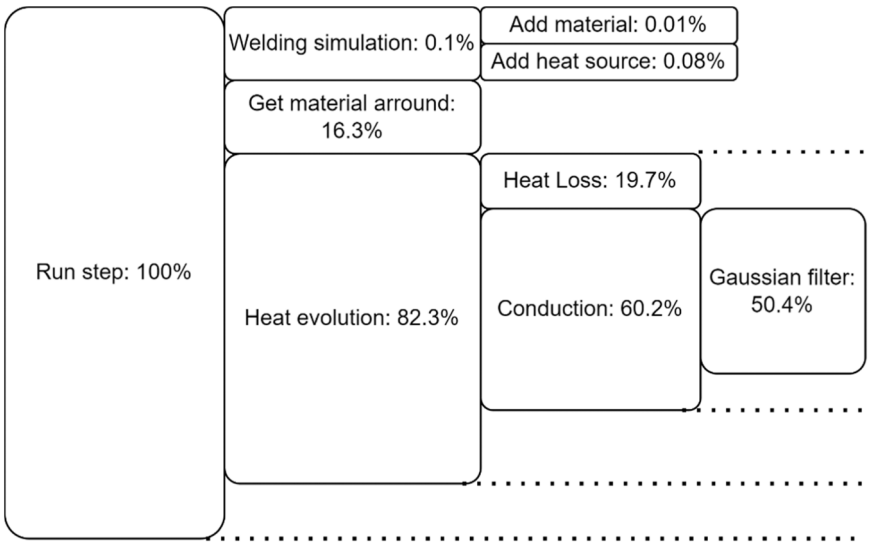

Fig. 12. Cumulative percentage of time for each function.

appropriate data structure, storing information solely for material elements, would speed up the neighborhood search (constituting 16 % of the computation time), and would also enable the use of alternative computation methods for convolution with the heat kernel.

5. Conclusion

This paper introduces a novel approach for rapid thermal simulation of the WAAM process, aiming to enhance the comparison of various manufacturing strategies such as trajectory, energy input, quantity of deposited material, by assessing their impact on the thermal state of the produced part to improve its overall quality. The proposed method has been described in detail and the various assumptions regarding the material and coefficient characteristics have been studied. Through comparison with experimental data, the accuracy appears to be largely satisfactory for optimizing manufacturing strategies. Computation times have been compared with common FEM simulation for the same studied case revealing that the proposed approach reduces computation time significantly—up to 80 times faster, and even faster than real-time WAAM operations. The influence of spatial and time discretization on model accuracy and calculation time has also been analyzed and led to a relevant compromise between calculation time and accuracy enabling WAAM process optimization in both offline and inline conditions. This paves the way for real-time optimization of operation by adjusting interlayer waiting times or the welding energy input according to the part geometry and manufacturing trajectory. The original main features of the proposed simulation are decoupling the calculation of the energy loss and the calculation of the conduction, the explicit matrix formulation of the solution and the use of kernel convolution for simulating conduction.

In this study a standard geometry (a thin wall) was used to able comparison with existing results in the literature. To access the model's robustness, it will be necessary to validate this model on more complex geometries. Numerical improvement regarding the data structure could also lead to drastic computing time reductions. The use of voxel can be

coupled with the adoption of non-matrix data structures like graphs could help to reduce calculation time (by reducing the number of zero-voxel manipulations) and facilitate the use of the method on more complex geometries. Such improvements should make it possible to create a rapid simulation tool that can be used on complex geometries, giving WAAM manufacturers a real competitive advantage.

CRediT authorship contribution statement

Franck Pourroy: Writing – review & editing, Writing – original draft, Supervision, Conceptualization. **Frédéric Vignat:** Methodology, Investigation, Conceptualization. **El-Haddi Mechekour:** Validation, Methodology, Investigation, Conceptualization. **Yann Ledoux:** Writing – review & editing, Writing – original draft, Validation, Methodology, Investigation, Formal analysis, Conceptualization. **Nicolas Béraud:** Writing – review & editing, Writing – original draft, Validation, Supervision, Software, Methodology, Investigation, Formal analysis, Conceptualization.

Declaration of Competing Interest

The authors declare that they have no known competing financial interests or personal relationships that could have appeared to influence the work reported in this paper.

Acknowledgements

This work was supported by ANR through the METALIC project ANR-20-CE10-0012, these supports are gratefully acknowledged.

References

[1] Pattanayak S, Sahoo SK. Gas metal arc welding based additive manufacturing—a review (mai) CIRP J Manuf Sci Technol 2021;vol. 33:398–442. https://doi.org/10.1016/j.cirpj.2021.04.010.
[2] Wu B, et al. A review of the wire arc additive manufacturing of metals: properties, defects and quality improvement. J Manuf Process oct. 2018;vol. 35:127–39. https://doi.org/10.1016/j.jmapro.2018.08.001.
[3] Béraud N, Chergui A, Limousin M, Villeneuve F, Vignat F. An indicator of porosity through simulation of melt pool volume in aluminium wire arc additive manufacturing. Mech Ind 2022;vol. 23:1. https://doi.org/10.1051/meca/2021052.
[4] Manokruang S, Vignat F, Museau M, Limousin M. " Process Parameters Effect on Weld Beads Geometry Deposited by Wire and Arc Additive Manufacturing (WAAM) " (in Lecture Notes in Mechanical Engineering). In: Roucoules L, Paredes M, Eynard B, Morer Camo P, Rizzi C, editors. Advances on Mechanics, Design Engineering and Manufacturing III. Cham: Springer International Publishing; 2021. p. 9–14. https://doi.org/10.1007/978-3-030-70566-4_3 (in Lecture Notes in Mechanical Engineering).
[5] Li R, Xiong J. Influence of interlayer dwell time on stress field of thin-walled components in WAAM via numerical simulation and experimental tests (janv) Rapid Prototyp J 2019;vol. 25(n° 8):1433–41. https://doi.org/10.1108/RPJ-03-2019-0067.
[6] Turgut B, Gürol U, Onler R. Effect of interlayer dwell time on output quality in wire arc additive manufacturing of low carbon low alloy steel components (juin) Int J Adv Manuf Technol 2023;vol. 126(n° 11):5277–88. https://doi.org/10.1007/s00170-023-11481-3.
[7] Zhang Y, Chen Y, Li P, Male AT. Weld deposition-based rapid prototyping: a preliminary study (avr) J Mater Process Technol 2003;vol. 135(n° 2-3):347–57. https://doi.org/10.1016/S0924-0136(02)00867-1.
[8] Rosli NA, Alkahari MR, Abdollah MF bin, Maidin S, Ramli FR, Herawan SG. Review on effect of heat input for wire arc additive manufacturing process (mars) J Mater Res Technol 2021;vol. 11:2127–45. https://doi.org/10.1016/j.jmrt.2021.02.002.
[9] Su C, Chen X, Gao C, Wang Y. Effect of heat input on microstructure and mechanical properties of Al-Mg alloys fabricated by WAAM (août) Appl Surf Sci 2019;vol. 486:431–40. https://doi.org/10.1016/j.apsusc.2019.04.255.
[10] Jorge VL, Teixeira FR, Scotti A. Pyrometrical interlayer temperature measurement in WAAM of thin wall: strategies, limitations and functionality. Art. n° 5, mai Metals 2022;vol. 12(n° 5). https://doi.org/10.3390/met12050765.
[11] Scotti A. The potential of IR pyrometry for monitoring interpass temperature in wire + arc additive manufacturing. EME sept. 2019;vol. 3(n° 1). https://doi.org/10.31031/EME.2019.03.000553.
[12] C. Cambon, S. Rouquette, I. Bendaoud, F. Soulie, " Estimation of the heat source parameters during the deposition of SS316L wire with GMAW-CMT process: application to additive manufacturing ", juin 2020.
[13] Dellarre A, Béraud N, Tardif N, Vignat F, Villeneuve F, Limousin M. Qualify a NIR camera to detect thermal deviation during aluminium WAAM (juill) Int J Adv Manuf Technol 2023;vol. 127(n° 1):625–34. https://doi.org/10.1007/s00170-023-11587-8.
[14] L. Jegou, J. Lachambre, N. Tardif, A. Zaoui, V. Kaftandjian, T. Elguedj, " Observation de la morphologie et cartographie thermique du bain fondu pendant la fabrication additive d'un mur en acier 316L par LMD-p ".
[15] García de la Yedra A, et al. Online cracking detection by means of optical techniques in laser-cladding process. Struct Control Health Monit 2019;vol. 26(n° 3):e2291. https://doi.org/10.1002/stc.2291.
[16] Hua Y, Choi J. Adaptive direct metal/material deposition process using a fuzzy logic-based controller. Art. n° 4 J Laser Appl nov. 2005;vol. 17(n° 4). https://doi.org/10.2351/1.2098811.
[17] Xia C, et al. A review on wire arc additive manufacturing: monitoring, control and a framework of automated system. J Manuf Syst 2020:15. https://doi.org/10.1016/j.jmsy.2020.08.008.
[18] " MetalWorm Software | Real Time Process Monitoring | Digital Twin ", MetalWorm. Consulté le: 11 septembre 2024. [En ligne]. Disponible sur: ⟨https://www.metalworm.com/software/⟩.
[19] Sandeep KJ, Teja PJ, Choudhary AK, Jain R. Development of correlation between temperature, liquid life span, molten pool, and porosity during Wire Arc Additive Manufacturing: A finite element approach (août) CIRP J Manuf Sci Technol 2022;vol. 38:274–87. https://doi.org/10.1016/j.cirpj.2022.05.002.
[20] Barath Kumar MD, Manikandan M. Assessment of process, parameters, residual stress mitigation, post treatments and finite element analysis simulations of wire arc additive manufacturing technique (janv) Met Mater Int 2022;vol. 28(n° 1):54–111. https://doi.org/10.1007/s12540-021-01015-5.
[21] Gokhale NP, Kala P. Thermal analysis of TIG-WAAM based metal deposition process using finite element method (janv) Mater Today: Proc 2021;vol. 44:453–9. https://doi.org/10.1016/j.matpr.2020.09.756.
[22] Montevecchi F, Venturini G, Scippa A, Campatelli G. Finite element modelling of wire-arc-additive-manufacturing process (janv) Procedia CIRP 2016;vol. 55:109–14. https://doi.org/10.1016/j.procir.2016.08.024.
[23] Wang X, Wang A. Three-dimensional finite element analysis with clamping in wire and arc additive manufacturing (nov) 2016 Eur Model Symp (EMS) 2016:104–8. https://doi.org/10.1109/EMS.2016.028.
[24] K.S. Reddy, " A computational approach to achieve uniform mechanical properties along the built-up direction in WAAM component ", A Dissertation Submitted to Indian Institute of Technology Hyderabad In Partial Fulfilment of the Requirements for The Degree of Master of Technology, Indian Institute of Technology Hyderabad, 2017.
[25] " Simufact Additive | Logiciels d'ingénierie assistée par ordinateur (logiciels IAO) ", Hexagon. Consulté le: 11 septembre 2024. [En ligne]. Disponible sur: ⟨https://hexagon.com/fr/products/simufact-additive⟩.
[26] Bauer A, Scharf R, Hälsig A, Awiszus B. Numerical simulation and calibration of a single seam WAAM process with a commercial and an open source software. Art. n° 1 J Appl Eng Des Simul sept. 2021;vol. 1(n° 1). https://doi.org/10.24191/jaeds.v1i1.21.
[27] Farias FWC, da Cruz Payão Filho J, Moraes e Oliveira VHP. Prediction of the interpass temperature of a wire arc additive manufactured wall: FEM simulations and artificial neural network (déc) Addit Manuf 2021;vol. 48:102387. https://doi.org/10.1016/j.addma.2021.102387.
[28] Zani M, Panettieri E, Montemurro M. A metamodel of the wire arc additive manufacturing process based on basis spline entities (janv) Eng Comput 2024. https://doi.org/10.1007/s00366-023-01926-4.
[29] Piercy NL, Kulkarni JD, Vishnu AS, Suryakumar S, Cole KD, Rao PK. Rapid thermal modeling of wire arc additive manufacturing process using a mesh-free spectral graph theory approach (août) Int J Adv Manuf Technol 2024;vol. 133(n° 11):5271–98. https://doi.org/10.1007/s00170-024-13994-x.
[30] Huang H, Ma N, Chen J, Feng Z, Murakawa H. Toward large-scale simulation of residual stress and distortion in wire and arc additive manufacturing (août) Addit Manuf 2020;vol. 34:101248. https://doi.org/10.1016/j.addma.2020.101248.
[31] Moreira CA, Caicedo MA, Cervera M, Chiumenti M, Baiges J. A multi-criteria h-adaptive finite-element framework for industrial part-scale thermal analysis in additive manufacturing processes (déc) Eng Comput 2022;vol. 38(n° 6):4791–813. https://doi.org/10.1007/s00366-022-01655-0.
[32] Essongue S, Ledoux Y, Ballu A. Speeding up mesoscale thermal simulations of powder bed additive manufacturing thanks to the forward Euler time-integration scheme: a critical assessment. Finite Elem Anal Des nov. 2022;vol. 211:103825. https://doi.org/10.1016/j.finel.2022.103825.
[33] Sampaio RFV, Pragana JPM, Bragança IMF, Silva CMA, Nielsen CV, Martins PAF. Modelling of wire-arc additive manufacturing – a review (mai) Adv Ind Manuf Eng 2023;vol. 6:100121. https://doi.org/10.1016/j.aime.2023.100121.
[34] Goldak J, Chakravarti A, Bibby M. A new finite element model for welding heat sources (juin) Met Trans B 1984;vol. 15(n° 2):299–305. https://doi.org/10.1007/BF02667333.
[35] Ling Y, Ni J, Abdel Wahab M, Antonissen J, Vande Voorde J. A Heat Transfer Finite Element Model for Wire-Arc-Additive-Manufacturing Process ", in *Proceedings of the 8th International Conference on Fracture, Fatigue and Wear*. In: Abdel Wahab M, editor. Lecture Notes in Mechanical Engineering. Singapore: Springer; 2021. p. 201–15. https://doi.org/10.1007/978-981-15-9893-7_14.
[36] Chergui A, Beraud N, Vignat F, Villeneuve F. " Finite Element Modeling and Validation of Metal Deposition in Wire Arc Additive Manufacturing ", in *Advances on Mechanics, Design Engineering and Manufacturing III*. In: Roucoules L, Paredes M, Eynard B, Morer Camo P, Rizzi C, editors. Lecture Notes in Mechanical

Engineering. Cham: Springer International Publishing; 2021. p. 61–6. https://doi.org/10.1007/978-3-030-70566-4_11.
[37] J.N. Dupont A.R. Marder, " Thermal Efficiency of Arc Welding Processes ".
[38] J.-B.-J. (1768–1830) A. du texte Fourier, *Théorie analytique de la chaleur, par M. Fourier*. 1822. Consulté le: 21 juin 2023. [En ligne]. Disponible sur: ⟨https://gallica.bnf.fr/ark:/12148/bpt6k1045508v⟩.
[39] El-Sayed MM, Shash AY, Abd-Rabou M. Finite element modeling of aluminium alloy AA5083-O friction stir welding process (févr) J Mater Process Technol 2018; vol. 252:13–24. https://doi.org/10.1016/j.jmatprotec.2017.09.008.
[40] Teng S, Dehgahi S, Henein H, Wolfe T, Qureshi A. Effect of surface texture, viewing angle, and surface condition on the emissivity of wire arc directed energy deposition manufactured 7075 nano treated aluminium alloy (mai) Int J Adv Manuf Technol 2023;vol. 126(n° 5):2175–89. https://doi.org/10.1007/s00170-023-11208-4.
[41] Limousin M, Manokruang S, Vignat F, Museau M, Grandvallet C, Béraud N. Effect of temperature and substrate geometry on single aluminium weld bead geometry deposited by wire arc additive manufacturing: proposition of an experimental procedure. CIRP J Manuf Sci Technol oct. 2023;vol. 45:61–8. https://doi.org/10.1016/j.cirpj.2023.06.010.